Compact Radiative Divertor Experiments at ASDEX Upgrade and Their Consequences for a Reactor

T. Lunt,[*] M. Bernert,[†] D. Brida, P. David, M. Faitsch, O. Pan, and D. Stieglitz

the ASDEX Upgrade team[‡]

Max Planck Institute for Plasma Physics, Boltzmannstrasse 2, 85748 Garching, Germany

U. Stroth

Physik-Department E28, Technische Universität München, 85747 Garching, Germany and Max Planck Institute for Plasma Physics, Boltzmannstrasse 2, 85748 Garching, Germany

A. Redl

Universitá degli Studi della Tuscia, DEIM, 01100 Viterbo, Italy

(Received 25 August 2022; accepted 2 March 2023; published 4 April 2023)

We present a novel concept to tackle the power exhaust challenge of a magnetically confined fusion plasma. It relies on the prior establishment of an X-point radiator that dissipates a large fraction of the exhaust power before it reaches the divertor targets. Despite the spatial proximity of the magnetic X point to the confinement region, this singularity is far away from the hot fusion plasma in magnetic coordinates and therefore allows the coexistence of a cold and dense plasma with a high potential to radiate. In the compact radiative divertor (CRD) the target plates are placed close to this magnetic X point. We here report on high performance experiments in the ASDEX Upgrade tokamak that indicate the feasibility of this concept. Despite the shallow (projected) field line incidence angles of the order of $\theta_\perp = 0.2°$, no hot spots were observed on the target surface monitored by an IR camera, even at a maximum heating power of $P_{\mathrm{heat}} = 15$ MW. And even with the X point located exactly on the target surface and without density or impurity feedback control, the discharge remains stable, the confinement good ($H_{98,y2} = 1$), hot spots absent, and the divertor in a detached state. In addition to its technical simplicity, the CRD scales beneficially to reactor-scale plasmas that would benefit from an increased volume of the confined plasma, more space for breeding blankets, smaller poloidal field coil currents, and—potentially—an increased vertical stability.

DOI: 10.1103/PhysRevLett.130.145102

The exploitation of nuclear fusion as a clean and abundant source of energy is one of the greatest ambitions of humankind. A nuclear fusion reactor is expected to produce about 2 GW of power from the nuclear fusion of deuterium and tritium, one fifth of which is transferred to the plasma via the electrically charged alpha particles. As long as the power is contained in charged particles it is bound to a high degree to the magnetic field. It is transported to the open field lines at the edge that intersect the inner walls of the reactor within an area on the order of $A = 1$ m^2, i.e., less than 1% of the total surface. Although the divertor, a region optimized for plasma-wall interaction, is designed to cope with large heat fluxes, it will not be able to handle the unmitigated and focused power flux of $q = P_\alpha/A = 400$ MW/m^2. The power exhaust challenge [1] intensively discussed in the community therefore consists of transferring a large fraction of the thermal energy from the plasma to unconfined neutral particles like photons, atoms, and molecules before reaching the divertor. The goal is to "detach" the plasma from the target, i.e., to reduce the flux of charged particles almost to zero [2,3].

Magnetic configurations alternative [4] to the conventional single-null (SN) divertor are currently being discussed as a candidate to facilitate the access to detachment [5–8]. These configurations, however, come at the price of additional magnetic coils with high currents and mechanical forces [9] and will likely reduce the cost effectiveness of the reactor substantially.

Here we pursue a new concept to tackle the problem, the "compact radiative divertor." It relies on the previous establishment of an X-point radiator (XPR) [10], a promising feature to achieve a high degree of dissipation, but in the conventional SN configuration. The magnetic X point defines the last closed flux surface in a tokamak, the boundary between the confinement region and the scrape-off layer (SOL). Despite its spatial proximity to the hot fusion plasma, this singularity is far away in both parallel and perpendicular directions of the magnetic field and therefore allows the existence of a cold and dense plasma with a high potential of radiative power dissipation. It was shown that overall more than 90% of the input power can be radiated in the plasma volume. The finding of the XPR regime can be seen as a change of paradigm in the community. While a movement of the radiation from the divertor to the X-point region previously was regarded to be dangerous and prevented under all circumstances, this effect is now deliberately exploited and actively controlled. The XPR configuration furthermore has other attractive features, like the strong reduction or even suppression of edge localized modes (ELMs), magnetohydrodynamic (MHD) instabilities [11] at the plasma edge that also threaten the exposed material surfaces. Small and frequent ELMs were observed to broaden the power deposition profile, while the peak power load is reduced [12,13] accordingly.

Recent experiments [14], an analytic model [15], and numerical simulations with SOLPS-ITER [16] have shown that the temperature inside the XPR can drop to a few eV such that volumetric recombination can contribute to power and momentum dissipation, similar to the conditions in a detached divertor.

This would allow one to place the X point close to the target, an idea previously identified to be unfavorable [17,18]. A CRD, combining an XPR with short divertor legs, would allow a reduced divertor size, an economically beneficial larger volume of the confined plasma, and a large poloidal flux expansion $f_x = ds_t/dr_u$, i.e., a large separation ds_t of neighboring flux surfaces at the target compared to their separation dr_u upstream. However, the related small (projected) field line incidence angles $\theta_\perp \propto f_x^{-1}$ at the target are regarded as a challenge [19]. Commonly, it is assumed that $\theta_\perp$ must be kept above about 2°, since otherwise magnetic error fields or small misalignments of the divertor tiles could lead to strong toroidal asymmetries in the power deposition pattern or even to the formation of hot spots. Also note that at grazing angles $\theta_\perp \lesssim 1°$ the classical sheath and magnetic presheath theory breaks down [20,21]. Recent simulations with the 3D transport code EMC3-EIRENE [8] show that at least error fields at shallow angles are not problematic if detachment can be guaranteed. This motivated the first CRD experiments at the ASDEX Upgrade (AUG) tokamak described in the following.

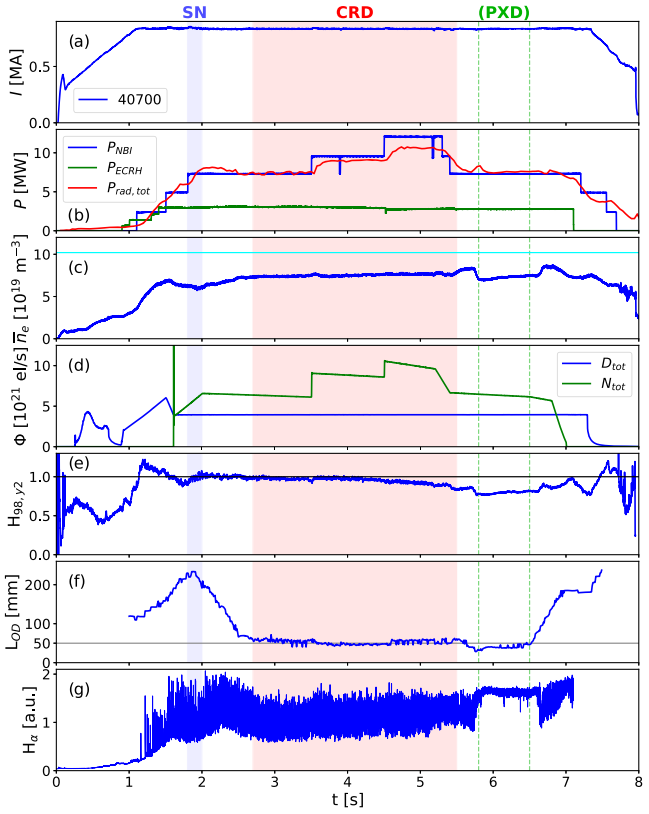

FIG. 1. Time traces of several quantities of discharge No. 40700. (a) Plasma current, (b) heating and radiation power, (c) lineaveraged density, (d) deuterium and nitrogen puff rates, (e) energy confinement time normalized to the ITER 98 scaling, (f) poloidal length of the outer divertor leg, (g) Balmer α line intensity in the upper divertor.

Figure 1 shows the time traces of several parameters of AUG discharge No. 40700 carried out at a plasma current of 830 kA [Fig. 1(a)]. It was heated by up to $P_{\mathrm{NBI}} = 12.5$ MW of neutral beam power and $P_{\mathrm{ECRH}} = 2.5$ MW of electron cyclotron heating [Fig. 1(b)]. The total radiative power loss $P_{\mathrm{rad,tot}}$ (red) is strongly influenced by the nitrogen impurities injected into the plasma [green curve in Fig. 1(b)], while the tungsten concentration is on the order of $c_W \sim 10^{-5}$ only. Shortly after 1 s, the plasma enters the high confinement mode (H mode) [22] as seen by the confinement factors $H_{98,y2}$ [Fig. 1(e)] [23] around unity and the appearance of ELMs visible as peaks in the D_α signal of the upper divertor [Fig. 1(g)]. Except for the very first ones, the ELMs are small and so frequent ($\gg 100$ Hz) that they are barely distinguishable. Figure 1(f) shows the poloidal length of the outer divertor leg L_{OD}, an indicator for the proximity of the X point to the target surface. For the conventional SN divertor, L_{OD} is determined by the condition of $\theta_\perp = 2°$ (for AUG $L_{\mathrm{OD}}^{2°} \approx 20$ cm). We distinguish three configurations: the SN, the CRD ($L_{\mathrm{OD}} \lesssim 5$ cm), and the PXD, where $L_{\mathrm{OD}} \to 0$. The first two are marked in Fig. 1 in blue and red, respectively.

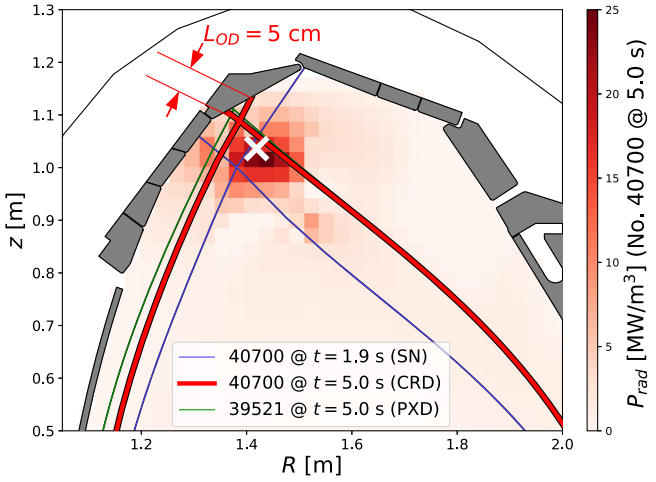

FIG. 2. X-point and separatrix positions for the SN (blue) and CRD (red) phases of No. 40700 (cf. Fig. 1) and the PXD (green), where the X point was located right on the target surface, of No. 39521. For the CRD case, the tomographic reconstruction of bolometry is underlayed showing an XPR. Its center of gravity is marked by the white cross.

The latter is an extreme case of the CRD, which was only marginally reached in No. 40700 (green), but almost ideally achieved in No. 39521, as seen in the magnetic configurations in Figs. 2 and 3.

Because of the nitrogen seeding [cf. Fig. 1(d) green], an XPR occurs in the early phase of the discharge. This XPR is still present and located inside the confinement region in the CRD configuration, as seen in the tomographic reconstruction of bolometry in Fig. 2.

In the following, the three configurations are compared with regard to their power exhaust properties. For this purpose, Fig. 3 shows the respective IR camera images, where the temperature distribution at the beginning of the discharge $T_{\mathrm{surf},0} = 373 \pm 30$ K was subtracted. The images are projected onto the computer aided design (CAD) drawings together with the separatrix and the inner and outer strike lines. The extension of the "near-SOL region," defined here as $\lambda = 1.5\lambda_q^{\mathrm{Eich}}$ mm, where $\lambda_q^{\mathrm{Eich}} = 3$ mm at the outboard midplane (OMP) [24,25] is also indicated in the figure by the thinner dash-dotted lines. The near SOL is regarded to be critical for power exhaust, while the far-SOL has been found to have a by far larger power falloff length [13].

From the measured temperature distribution, one cannot directly deduce the heat flux, but one can see that no hot spots are developing. The peak temperatures are measured at the tile edges: due to the tile gap and the flat tile geometry, the corners are not shadowed by the neighboring tiles. The maximum absolute temperatures in the near SOL are $T_{\mathrm{surf}}^{\mathrm{max}} = \Delta T_{\mathrm{surf}}^{\mathrm{max}} + T_{\mathrm{surf},0} = 627 + 373$ K $= 1000$ K for the SN and are reducing to 824 K (at 10 MW of external heating) or 907 K (at 15 MW) for the CRD, despite the lack of active cooling of the tiles, indicating that the heat flux is significantly reduced. For the PXD phase, $T_{\mathrm{surf}}^{\mathrm{max}}$ is even lower at 661 K. Note that higher temperatures outside the near SOL might occur due to the nonoptimized geometry. The measured temperatures are far away from the recrystallization temperature of tungsten [26] around 2000 K and even further from its melting point at 3695 K. With the known 3D viewing geometry of the camera, cylindrical coordinates R, z, and ϕ of the surface position are assigned to each pixel. For every time step and every observed divertor tile, the toroidally averaged temperature was computed and used as an input for the heat diffusion

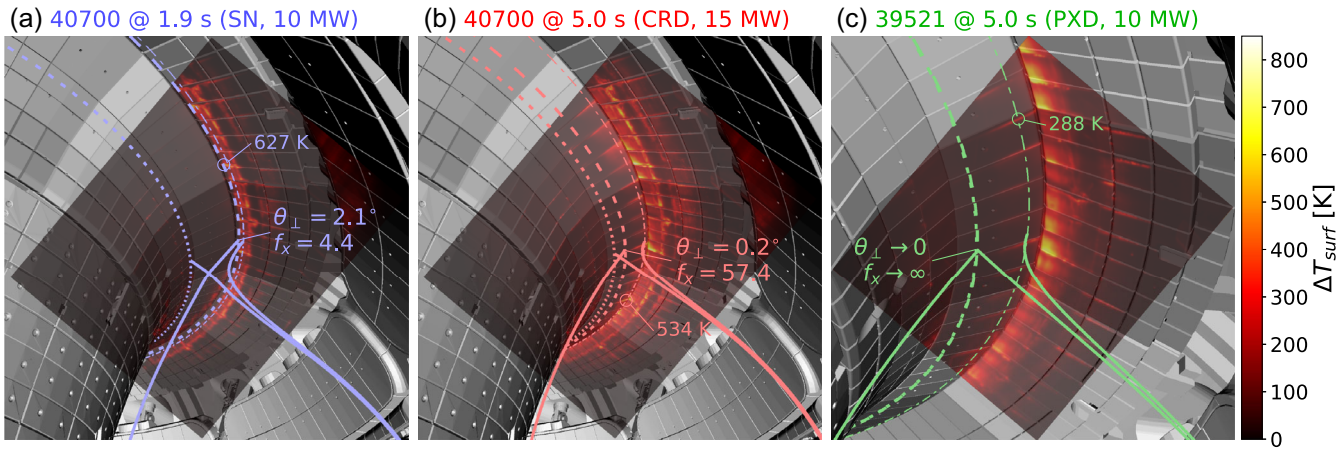

FIG. 3. Surface temperature rise $\Delta T_{\mathrm{surf}} = T_{\mathrm{surf}} - T_{\mathrm{surf},0}$ since the beginning of the discharge ($T_{\mathrm{surf},0} = 373 \pm 30$ K) measured by IR thermography. The 2D camera images are projected onto 3D AUG CAD construction drawings together with the magnetic separatrix (solid lines) and the inner (dotted) and outer (dashed) strike line, while the near-SOL region extends up to the dash-dotted line. The conventional SN configuration in (a) is compared to the compact radiative divertor (CRD) in (b). (c) An extreme case of the CRD, the primary X-point divertor (PXD), where the strike lines coincide with the X point. Despite the shallow field line angles $\theta_\perp \leq 0.2°$ in (b) and (c) no detrimental hot spots are observed in the near SOL and the configurations remain stable.

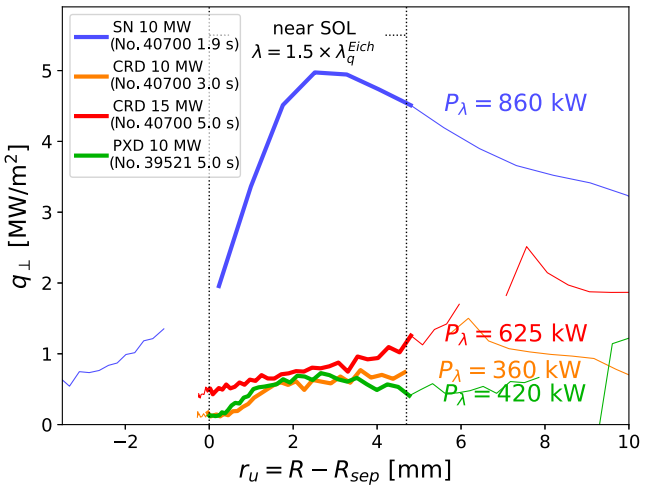

FIG. 4. Toroidally averaged heat flux to the upper outer target as a function of the upstream coordinate r_u for the different configurations shown in Figs. 2 and 3. Note the strong variation of the flux expansion $f_x = ds_t/dr_u$ for the different cases. The integral values P_λ over the target coordinate s_t in the near SOL are given in the figure.

simulation code THEODOR [27] in order to reconstruct the (toroidally averaged) heat deposition profiles $q_\perp(R,t)$ shown in Fig. 4. Note that the field of view (FOV) of the IR camera was optimized for a large toroidal coverage $\Delta\phi = 70°$ or $L = 1.8$ m. This is to avoid screening effects from misaligned tiles. To shadow the full FOV, a tile outside the FOV would need to protrude by more than $L\tan\theta_\perp = 6$ mm. The maximum misalignment was measured to be 1.7 mm at a location more than $\Delta\phi = 90°$ away from the FOV, while the average misalignment is 0.6 mm. Therefore, the measured $q_\perp(R,t)$ is representative for the overall toroidal average.

Spatiotemporal integrals are computed for every tile and the resulting energies are compared to measurements from thermocouple calorimetry, deviating by less than 35%. Spatial integrals $P_\lambda = \int q_\perp 2\pi R ds_t$ over the near-SOL region are also computed along the target coordinate s_t. As seen in Fig. 4, the maximum $q_\perp$ value reduces by a factor of more than 6 when changing from the SN to the CRD configuration at $P_{\text{heat}} = 10$ MW, partly caused by the larger average flux expansion. The integrated value P_λ decreases from 860 to 360 kW. This still contains the contribution from radiation that was estimated as 43 kW in the SN case and 275 kW in the CRD. So the power deposited by charged particles in the near SOL is reduced by a factor of about 10, indicating a substantial reduction of $q_{||}$.

While the divertor Langmuir probes indicate temperatures in the range 5–10 eV in the SN phase, this is significantly lower in the CRD phase. Also the strong reduction of P_λ indicates that the near SOL in the CRD is detached. It is a remarkable achievement that stable and pronounced detachment can be sustained in the CRD even without feedback control of the impurity seeding or the density.

Even at the aforementioned position of the maximum tile misalignment of 1.7 mm, only a moderate glow, but no hot spot, was observed by a visible overview camera. This proves that the CRD can even tolerate such a significant misalignment, which is substantially above the foreseen tolerances for a reactor. Furthermore, under these conditions, the "optical hot spots" that are included in the present ITER design [28] and that were recently observed experimentally in the WEST tokamak [29] might not be a problem.

An explanation for the high exhaust capabilities of the CRD could be that the volume V_X of the vicinity of the X point with a given minimum parallel connection length to the OMP (here $L_c = 15$ m) [15] is 60% larger than in the SN. Another explanation might be a high "plugging" of the neutrals by the plasma [30] near the strike lines due to the large flux expansion. The presence of neutral particles in the XPR was also found to be essential [15] and further improves the radiative capabilities of the impurities via charge exchange reactions [31].

In the shown experiments, the CRD has a slightly higher radiative fraction (80% compared to 75%) and a higher density (72% instead of 60% of the Greenwald density $n_{\text{GW}} = 1.02 \times 10^{20}$ m^{-3} [32], cyan line in Fig. 1) than the SN. The confinement ($H_{98,y2} = 0.98$) was not affected when going from SN to CRD in discharge No. 40700 and only decreased slightly ($H_{98,y2} = 0.92$) at $t = 5$ s, most likely due to MHD activity ($n = 2$, $m = 3$). Discharge No. 39521, where no MHD modes were present, has a confinement even slightly above $H_{98,y2} = 1$.

The CRD configuration has very attractive properties for a fusion reactor. As an example, we here refer to the 2019 European DEMO design described in [33]. The movement of the X point toward the target obviously enhances the volume of the confined plasma, one of the most important optimization parameters for a reactor. This movement is achieved by reducing the current I_{div} in the divertor coil, in this example by 50%. While in a reactor this effect is expected to be less pronounced, it can nevertheless lead to a significant reduction of the conductor and support material of the poloidal field (PF) coils. A reduction of the divertor coil current is also beneficial for the vertical stability and thus reduces the risk of vertical displacement events, one of the most severe threats for DEMO [34]. A larger poloidal plasma cross section can also enhance the inductive current drive efficiency.

The radial extension of the XPR volume mapped to the OMP is only a few hundred micrometers in AUG, a value clearly smaller than λ_q^{Eich}. Since L_c scales linearly with the machine size, the same is expected for $\Delta r_{u,\text{XPR}}$ and would be $f_{AD} = R_{\text{DEMO}}/R_{\text{AUG}} = 9/1.65 = 5.45$ times larger than in AUG, while λ_q^{Eich} is expected even to decrease [24]. The X-point region in DEMO therefore is expected to have a far higher relevance for power exhaust than in an AUG size tokamak. Stroth *et al.* [15] also pointed out the

importance of neutral particles in the X-point region. Since the mean free path for ionization in DEMO is expected to decrease rather than to increase, it might actually be *necessary* to place the X point close to the target to access the XPR regime.

Even though the directed heat load of charged particles $q_{||}$ might vanish almost completely in the CRD configuration, the power loads from radiation q_{rad} might become a concern. As a worst-case estimate, the XPR is approximated by a single ring filament with no poloidal extension converting the full exhaust power of the reactor $P_{\mathrm{exh}} = 450$ MW into radiation. A maximum value of $q_{\mathrm{rad}} = P_{\mathrm{exh}}/(4\pi^2 d_{\mathrm{XPR}} R_{\mathrm{XPR}} f_{AD}^2) = 3.0\ \mathrm{MW/m^2}$ is found, where the radius $R_{\mathrm{XPR}} = 1.42$ m and the distance $d_{\mathrm{XPR}} = 89$ mm from the wall are taken from AUG (cf. white cross in Fig. 2) and both scaled linearly by the aforementioned factor f_{AD}. This is well below the material limit of $10\ \mathrm{MW/m^2}$.

Furthermore, a viable path from the startup to the CRD configuration has to be found for a reactor. It could be done similarly like shown here: First establishing the XPR in SN and then move to the CRD. Or a CRD could be established directly after the startup by a carefully controlled balance between heating power and seeding ramps. For the latter, detachment has to be assured during the transition from the low to the high confinement regime, which was recently achieved in lower SN discharges. Reattachment during transient excursions of the exhaust power also has to be avoided. This was tested at AUG in the lower divertor. Here the location of the XPR acts as a fast buffer for heat pulses 75% above the stationary heating power. The active control of the XPR location can then act fast enough to avoid reattachment.

The required high levels of impurity seeding in the plasma (2%–3% core nitrogen concentration for AUG) are an additional concern for DEMO. While the ignition of a reactor is still viable at these levels [35], it might limit the operational space. However, since the impurity transport in a reactor will be quite different to that in AUG [36], linear scalings are not applicable and transport modeling is required.

Further research will be devoted to the question of how to realize a pumping concept for He-ash removal in the CRD. Experiments in the lower divertor, where the according diagnostics are available, indicate that the neutral compression remains high ($p_{0,\mathrm{div}}/p_{0,\mathrm{main}} > 200$) in the CRD configuration, which most likely facilitates He pumping.

In conclusion, a novel divertor concept, the CRD configuration was successfully tested and characterized in AUG. The CRD configuration was sustained for up to 3 s even without feedback control mechanisms at a maximum total heating power of 15 MW, at a good confinement, and without large ELMs. Despite the very shallow field line incidence angles of $\theta_{\perp} \lesssim 0.2°$ no hot spots were observed on the target plates in the field of view of the IR camera. This is attributed to a substantial reduction of the parallel heat flux density $q_{||}$ in the detached divertor state. The CRD configuration has further attractive properties for a reactor, in particular, a much simpler divertor structure and lower material loads, a large poloidal flux expansion, a larger volume of the confined plasma, reduced forces between the PF coils and potentially an enhanced vertical stability. In particular, the importance of the X-point radiator seems to scale beneficially to a large machine. A series of challenges have been identified and discussed, but none of them is regarded to be a show stopper. If these challenges can be overcome, the CRD configuration could be a potential game changer for a reactor, easing its design and significantly reducing the costs.

This work has been carried out within the framework of the EUROfusion Consortium, funded by the European Union via the Euratom Research and Training Programme (Grant Agreement No. 101052200—EUROfusion). Views and opinions expressed are, however, those of the author(s) only and do not necessarily reflect those of the European Union or the European Commission. Neither the European Union nor the European Commission can be held responsible for them.

*tilmann.lunt@ipp.mpg.de
†matthias.bernert@ipp.mpg.de
‡See author list of U. Stroth *et al.*, Nucl. Fusion 62, 042006 (2022).

[1] A. Loarte and R. Neu, Fusion Eng. Des. **122**, 256 (2017).
[2] M. Keilhacker *et al.*, *Plasma Physics and Controlled Nuclear Fusion Research* (IAEA, Vienna, 1982), Vol. 3, p. 183.
[3] A. Kallenbach *et al.*, Nucl. Fusion **55**, 053026 (2015).
[4] V. A. Soukhanovskii, Plasma Phys. Controlled Fusion **59**, 064005 (2017).
[5] H. Reimerdes *et al.*, Nucl. Fusion **57**, 126007 (2017).
[6] C. Theiler *et al.*, Nucl. Fusion **57**, 072008 (2017).
[7] O. Pan, T. Lunt, M. Wischmeier, and D. Coster, Plasma Phys. Controlled Fusion **60**, 085005 (2018).
[8] T. Lunt *et al.*, Nucl. Mater. Energy **26**, 100950 (2021).
[9] H. Reimerdes *et al.*, Nucl. Fusion **60**, 066030 (2020).
[10] M. Bernert *et al.*, Nucl. Fusion **61**, 024001 (2020).
[11] H. Zohm, Plasma Phys. Controlled Fusion **38**, 105 (1996).
[12] M. Faitsch *et al.*, Nucl. Mater. Energy **26**, 100890 (2021).
[13] T. Lunt *et al.*, Plasma Phys. Controlled Fusion **62**, 105016 (2020).
[14] M. Cavedon *et al.*, Nucl. Fusion **62**, 066027 (2022).
[15] U. Stroth, M. Bernert, D. Brida, M. Cavedon, R. Dux, E. Huett, T. Lunt, O. Pan, and M. Wischmeier (the ASDEX Upgrade Team), Nucl. Fusion **62**, 076008 (2022).
[16] O. Pan *et al.*, Nucl. Fusion **63**, 016001 (2023).
[17] D. Hill *et al.*, Controlled fusion and plasma physics, in *Proceeding of 20th Europe Conference* (EPS, Lisbon, Portugal, 1993), Vol. 17C, p. 643.
[18] C. J. Lasnier, D. N. Hill, T. W. Petrie, A. W. Leonard, T. E. Evans, and R. Maingi, Nucl. Fusion **38**, 1225 (1998).
[19] T. Lunt *et al.*, Nucl. Mater. Energy **12**, 1037 (2017).

[20] D. Tskhakaya and S. Kuhn, J. Nucl. Mater. **313**, 1119 (2003).
[21] G. F. Matthews, S. J. Fielding, G. M. McCracken, C. S. Pitcher, P. C. Stangeby, and M. Ulrickson, Plasma Phys. Controlled Fusion **32**, 1301 (1990).
[22] F. Wagner *et al.*, Phys. Rev. Lett. **49**, 1408 (1982).
[23] ITER Physics Expert Group, Nucl. Fusion **39**, 2175 (1999).
[24] T. Eich, B. Sieglin, A. Scarabosio, W. Fundamenski, R. J. Goldston, and A. Herrmann, Phys. Rev. Lett. **107**, 215001 (2011).
[25] M. Siccino, G. Federici, R. Kembleton, H. Lux, F. Maviglia, and J. Morris, Nucl. Fusion **59**, 106026 (2019).
[26] J.-H. You, M. Li, and K. Zhang, Fusion Eng. Des. **164**, 112203 (2021).
[27] A. Herrmann, W. Junker, K. Gunther, S. Bosch, M. Kaufmann, J. Neuhauser, G. Pautasso, Th. Richter, and R. Schneider, Plasma Phys. Controlled Fusion **37**, 17 (1995).
[28] J. Gunn *et al.*, Nucl. Fusion **57**, 046025 (2017).
[29] M. Diez, J. P. Gunn, M. Firdaouss, A. Grosjean, Y. Corre, E. Delmas, L. Gargiulo, and E. Tsitrone, Nucl. Fusion **60**, 054001 (2020).
[30] L. Casali, C. Sang, A. L. Moser, B. M. Covele, H. Y. Guo, and C. Samuell, Contrib. Plasma Phys. **58**, 725 (2018).
[31] R. Dux, M. Cavedon, A. Kallenbach, R. M. McDermott, and G. Vogel (the ASDEX Upgrade team), Nucl. Fusion **60**, 126039 (2020).
[32] M. Greenwald, Plasma Phys. Controlled Fusion **44**, R27 (2002).
[33] G. Federici, Fusion Eng. Des. **178**, 113103 (2022).
[34] F. Maviglia *et al.*, Nucl. Mater. Energy **26**, 100897 (2021).
[35] T. Pütterich, E. Fable, R. Dux, M. O'Mullane, R. Neu, and M. Siccinio, Nucl. Fusion **59**, 056013 (2019).
[36] R. Dux *et al.*, Nucl. Mater. Energy **12**, 28 (2017).